atmosphere

MDPI

Article

Comparison of Cold Pool Characteristics of Two Distinct Gust Fronts over Bohai Sea Bay in China

Changyi Xu [1,2,3,*] and Xian Xiao [4]

[1] Binhai New Area Meteorological Office of Tianjin, Tianjin 300450, China
[2] Key Laboratory of Urban Meteorology, China Meteorology Administration, Beijing 100089, China
[3] Institute of Atmospheric Environment, China Meteorology Administration, Shenyang 110166, China
[4] Institute of Urban Meteorology, China Meteorology Administration, Beijing 100089, China; xxiao@ium.cn
* Correspondence: xusupergirl@163.com

Abstract: Previous studies have demonstrated that cold pools play a pivotal role in the initiation and organization of convection, yet their influence on the evolution of gust fronts (GFs) remains inadequately understood. A destructive wind event associated with a rearward gust front (RGF; 8 grade gale after passing GF) and a prior gust front (PGF; 10 grade gale before passing GF) over the north coast of China on 10 June 2016 was analyzed. Using multiple forms of observation data, as well as the four-dimensional Variational Doppler Radar Data Assimilation System (VDRAS), we found that the depth and intensity of the cold pool in RGF are relatively shallower and weaker, leading to a correspondingly reduced strength in both outflow and convergence. In contrast, the enhanced vertical shear and boundary northeaster inflow of PGF generate intensified and more organized downdrafts, resulting in a deeper cold pool, robust outflow, and convergence. Two schematic models were proposed to explain the discrepancy between GFs and associated cold pools. We further show that there is an internal correlation between meso-γ-scale vortices (MVs) and cold pools, the collision of MVs strengthened low-level convergence and updraft between these two GFs. Moreover, the consolidation of the two cold pools exacerbates low-layer instability and rotation, generating an intense horizontal vorticity that leads to rapid convective storm intensification. These findings offer novel insights into the diversity of GFs and associated cold pools.

Keywords: gust fronts (GFs); cold pool; vertical wind shear; meso-γ-scale vortices (MVs); VDRAS

check for updates

Citation: Xu, C.; Xiao, X. Comparison of Cold Pool Characteristics of Two Distinct Gust Fronts over Bohai Sea Bay in China. *Atmosphere* **2024**, *15*, 247. https://doi.org/10.3390/atmos15030247

Received: 11 January 2024
Revised: 10 February 2024
Accepted: 12 February 2024
Published: 20 February 2024

Copyright: © 2024 by the authors. Licensee MDPI, Basel, Switzerland. This article is an open access article distributed under the terms and conditions of the Creative Commons Attribution (CC BY) license (https://creativecommons.org/licenses/by/4.0/).

1. Introduction

One major marine meteorological disaster is thunderstorm gales [1]. These refer to ground-level wind with speeds equal to or exceeding 17.2 $m \cdot s^{-1}$, resulting from convective storms [2]. Thunderstorm gales often lead to significant human casualties and substantial economic losses [3,4].

The gust fronts (GFs), which are closely associated with convective storms, are defined as the boundary between the cold downdraft outflow propagated horizontally by the convective storm and the ambient air [5–7]. The GFs not only act as a factor triggering the releases of convective energy to the boundary layer [8–10], but also play an important role in the localization and evolution of convective storms [11–13]. Historically, research on the characteristics of GFs has predominantly focused on the quasi-linear convective system (QLCS) and bow echo (BE) [14–16]. However, little work has investigated two different types of GFs along convective cells (CCs [2]). Therefore, the thermodynamic structures of GFs, as well as the surface cold pool, are analyzed in this study, which has a positive impact for understanding the regularities of disastrous weather and enhancing the early warning capabilities.

As the leading edge of the strong outflow from thunderstorms, GFs are often accompanied by meteorological phenomena, such as pressure rises, wind shifts, wind surges,

temperature drops, and especially strong winds that occur at the surface [17–19]. There are obvious ground divergences, which appear behind the GFs, while the convergences appear in front of it [20,21]. Close to the GFs, an upward movement can be measured [22,23], and there are significant differences in the thermal and dynamical structures of GF between the cases with and without precipitation [24]. GFs typically exhibit depths ranging from 0.5 to 2.0 km, although this range can vary between 100 m and 4 km depending on the intensity and proximity to the downdraft source [25]. By utilizing the radar data, Martner [26] observed that the GF achieved a maximum ascending speed of 10 $m \cdot s^{-1}$ at an altitude of 1.35 km, which was subsequently followed by a rapid descent after one min, indicating a sudden transition between the strong ascending and descending motions near the GF.

From the GFs' maintaining mechanisms perspective, the significance of cold pool and low-level environmental wind shear in the perpetuation of thunderstorms has been a subject of concern [27]. According to the Rotunno Klemp Weisman (RKW) theory (hereafter RKW88 [28]), the interaction between vertical wind shear ahead of thunderstorms and the cold pool formed by convective precipitation can directly influence the uplift of ambient air at the leading edge of the cold pool (near the outflow boundary), thereby determining the formation of new convective cells, as well as various aspects related to the maintenance, development, propagation, and evolution of the entire convective system [28–30]. Weckwerth and Wakimoto [31] observed that GF updraft maxima occurred on the upshear side of Kelvin–Helmholtz waves, intersecting the boundary at altitudes approximately 1–2 km above the surface, with angles close to 90° and intervals ranging from 3 to 5 km. Regrettably, the available data were insufficient to substantiate a causal relationship between these maxima and storm initiation. Kingsmill [32] observed a sequence of small-scale (2–4 km) vertical vorticity maxima, evenly spaced at intervals of 3–5 km along an intense GF. It was noted that the GF was affected by Kelvin Helmholtz instability (KHI), which is conducive to the strengthening of ascending motion and the maintenance of thunderstorms. Furthermore, meso-γ-scale vortices (MVs) tend to appear at the position of strong shear along the GFs [33,34]. The presence of moderate-to-strong vertical wind shear at low to mid-levels was found to be conducive to the formation of robust, deep, and long-lasting mesoscale vortices (MVs). Additionally, the Coriolis force and the presence of strong cold pools were also identified as favorable factors for the genesis of vigorous MVs [35].

Convectively generated cold pools constitute an integral component of the convective storm cycle. These cold pools result from downdrafts that are latently cooled and subsequently reach the surface, spreading outward in a manner often referred to as a density current [36]. As they displace the surrounding warm, moist air, this phenomenon can be described as a convective-induced density current [15]. In conjunction with the ambient wind shear, cold pools contribute to the uplift of surrounding air parcels and facilitate the formation of new cells, thereby organizing mesoscale convective systems (MCSs) [37,38]. Consequently, cold pools play a pivotal role in organizing deep convection and are an indispensable component of MCSs [39,40].

Weckwerth and Wakimoto [31] were the first to quantitatively analyze the initiation of convection by a single GF atop the cold-air outflow, highlighting that the combined motion of Kelvin Helmholtz (K-H) and internal gravity (IG) waves exhibited consistent behavior with convective cell movement. According to density current theory [41], the compensatory relationship between cold pool density and depth results in a nearly constant speed for the leading edge of the cold pool (LECP), despite the diminishing strength and varying height of the cold pool over time [42]. The forced mechanical lifting induced by the collision of cold pools within gust fronts can initiate convective processes and is particularly intensified during multi-cold pool collisions [43]. The updrafts and mass flux exhibit a significant enhancement in multi-cold pool collisions compared to single cold pool gust fronts [44].

The previous results provide references that allow for an understanding of the necessary conditions for the formation of GF gales and enhance the ability to forecast and the warning time. However, studies of cold pools are still missing in some regions (e.g., North

China) where the influences of GFs and cold pools are also significant. Many important questions about GFs and cold pools still remain to be answered, including the following:

(1) Why do GF gales occur in some environments but not in others? What environmental parameters determine the potential for GF gales?
(2) What is the relationship between strength in GFs and cold pools? What is the potential role of cold pools in the evolution of GFs?

This paper is an attempt to answer these ongoing questions with the help of various kinds of meteorological data from over the Bohai Sea Bay (BSB), China. On 10 June 2016, from 06:00 UTC to 18:00 UTC, two strong wind events triggered by consecutive GFs along convective cells (CCs) occurred over the BSB. The maximum wind speed observed by the national automatic station was 26.0 m·s^{-1} (grade 10, at 12:51 UTC), while the regional station record was 32.6 m·s^{-1} (grade 11, at 13:46 UTC). Figure 1b shows the distribution of instantaneous wind speed (≥17.2 m·s^{-1}) during 06:00–18:00 UTC at the national automatic station on June 10. Abulikemu et al. [45] investigated the convection initiation (CI) mechanism associated with GFs generated by MCS in this particular case. This paper focuses on the differences between the evolutions, as well as the implications of cold pools on the evolution of the two GFs.

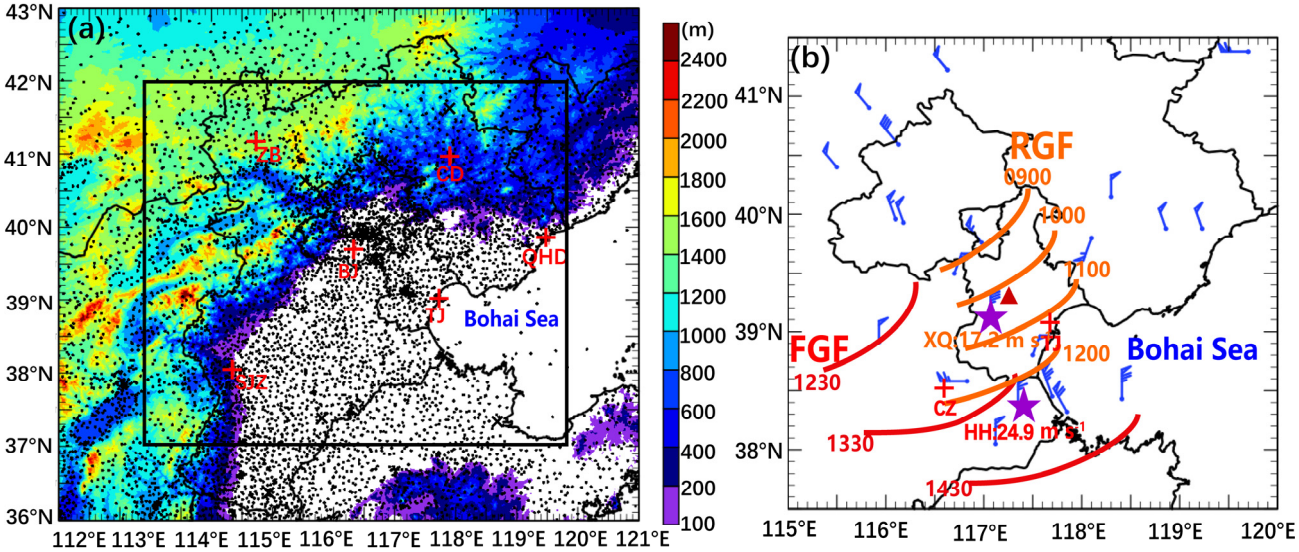

Figure 1. (**a**) Domain of North China and terrain heights (shading, unit: m). The solid black rectangle represents the domain of the Variational Doppler Radar Assimilation and Analysis System (VDRAS). The estuary in the west of the Bohai Sea is called the Bohai Sea Bay (BSB). The six radar sites of the operational China New Generation Radars (CINRAD) network are indicated (+symbols) as follows: BJ, TJ, SJZ, ZB, CD, and QHD. The black dots represent automatic weather stations (AWSs). (**b**) Tracked gust fronts and analysis of the spatial distribution of the maximum observed gust winds in the Bohai area from 06:00 to 18:00 UTC on 10 June 2016. The orange and red lines indicate the tracks of rearward GF (RPG) and frontward GF (FGF), respectively. The orange and red font represent the time of RPF and FGF, respectively. TJ (CZ): Tianjin (Cangzhou) Doppler radar. The purple "★" denote the position of Xiqing (XQ) and Huanghua (HH) wind profiles. The red "▲" shows the position of the meteorological tower.

2. Data and Methods

2.1. Reanalyzed and Observation Data

The pre-convective synoptic environments were examined using the fifth-generation European Center for Medium-Range Weather Forecast reanalysis (ERA5; Hersbach et al. [46]). The spatial resolution of ERA5 is 0.25° with a 1 h temporal interval. The radar data used in this paper are from two WSR/98D Doppler weather radars (Figure 1b), located in Tanggu

(39.04° N, 117.72° E) of Tianjin and Cangzhou (38.28° N, 116.08° E) of Hebei Province. The radars operate with a scanning radius of 230 km, a volume scanning cycle of 6 min, and scanning elevations within 0.5°–19.5°. The surface automatic weather station (AWS) data recorded at an interval of 1 h, including 2 m temperature, 2 m dew-point temperature, surface pressure, 10 m average winds and transient winds at the elevation of station height, were used to analyze the near-surface processes before and during this event.

2.2. Description of VDRAS

The VDRAS system is a rapid-update, four-dimensional, variational (4DVAR) data assimilation system constrained by a cloud model (Sun and Crook, [47,48]). It includes a three-dimensional cloud model, equations for the prediction of precipitation, an adjoint assimilation model, cost function, and a recursive minimization algorithm. In addition to its use as a research tool for convective-scale analyses (Friedrich et al. [49]; Tai et al. [50]), VDRAS has been used for operational nowcasting in several forecasting offices (Crook and Sun, [51]; Sun et al. [52]). The surface observation data used in this study were surface automatic weather station (AWS) data recorded at an interval of 1 hr. The radar data from six S-band China New Generation Radars (CINRADs) located at Beijing (BJ), Tianjin (TJ), Shijiazhuang (SJZ), Zhangbei (ZB), Chengde (CD), and Qinhuangdao (QHD) were assimilated into the VDRAS (see Figure 1a for the locations of radars). These six radars were run operationally in the same scan mode to detect reflectivity and radial velocities at nine elevation angels (0.5°, 1.5°, 2.5°, 3.4°, 4.4°, 6.1°, 9.9°, 14.6°, and 19.6°) with a volume scan rate of 6 min. The mesoscale forecast data from the National Center for Atmospheric Research's Weather Research and Forecast (WRF) model were used for first guesses and boundary conditions. The 4DVAR-based VDRAS seeks an optimal initial state with the smallest difference between model forecasts and observations within a short assimilation window (Sun [53]). In this study, we used a 12 min window in which at least two radar volume scans from each of the six radars were assimilated to provide an accurate convective-scale analysis. The first guess and boundary conditions for VDRAS were WRF forecasts from the operational 3-h cycle of WRF products produced by Beijing Meteorological Services.

The domain for the VDRAS analysis was 540 km × 540 km with a 5 km horizontal resolution centered at 39.58936° N, 116.1802° E (Figure 1a). The vertical depth of the VDRAS analysis was 15 km with a 400 m vertical resolution and 30 layers. Several previous studies have evaluated the accuracy of VDRAS analyses of wind and temperature fields against wind profiler data and AWS data (Chen et al. [54]; Xiao et al. [55]). The reliability of the 4DVar model's inversion results has been verified (Chen et al. [54]). These studies found that VDRAS wind and temperature analyses yielded a reasonable agreement with observations made in severe weather situations for different regions of the world (Wu et al. [56]; Zhang et al. [57]; Xiao et al. [58]; Cui et al. [7]).

3. Synoptic Conditions and Environment Conditions

The synoptic pattern before the formation of GFs is shown in Figure 2 according to ERA5. The 500 hPa geopotential height chart (Figure 2a) shows a cold vortex in the Northeast China, and BSB lies in the westerly flow in front of an upper trough at 09:00 UTC 10 June 2016. The westerly flow increased from 20 $m \cdot s^{-1}$ at 06:00 UTC (figure omitted) to 24 $m \cdot s^{-1}$ at 09:00 UTC, and the cold advection increased in the afternoon. The temperature gradient between 850 and 500 hPa in BSB increased to 30–32 °C, indicating an enhanced vertical lapse rate. Furthermore, the warm and wet advection in front of the lower trough at 850 hPa caused instability in the cold air at the upper level and warm air at the lower level (Figure 2b), so it is a reasonably favorable synoptic condition for the development of the convective storm.

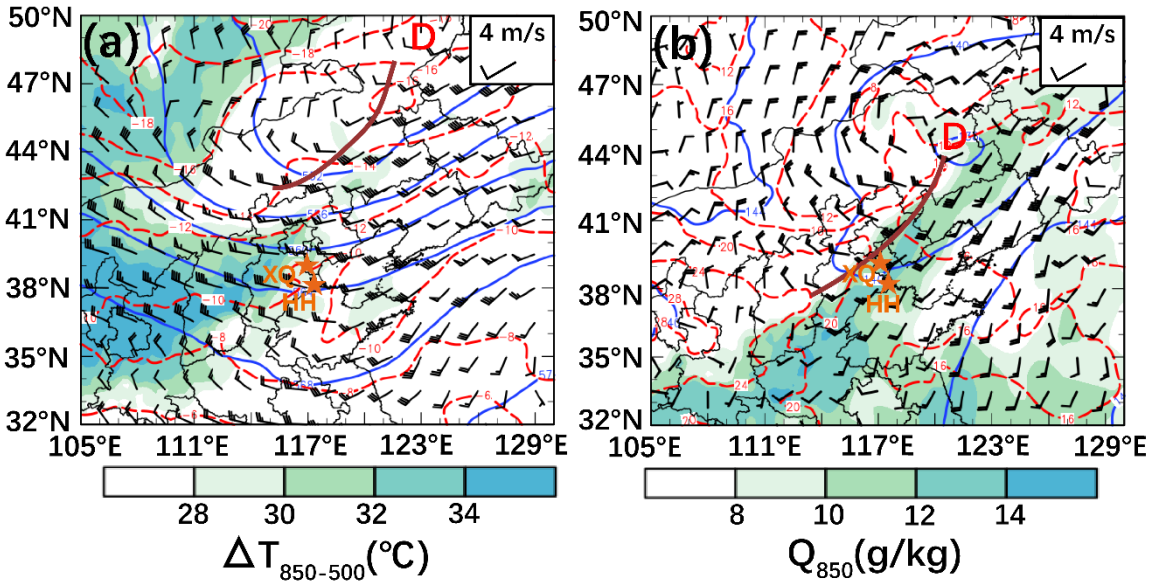

Figure 2. Synoptic setting at 09:00 UTC 10 June 2016. (**a**) Geopotential height (blue solid line, unit: dagpm), temperature (red dashed line, unit: °C), and wind (barb, unit: m·s^{-1}) at 500 hPa (**a**) and 850 hPa (**b**); temperature difference between 850 and 500 hPa (a, shading, unit: °C), specific humidity ((**b**), shading, unit: g·kg^{-1}). The brown line represents the shear line. D: low pressure; "★" denotes the positions of Xiqing (XQ) and Huanghua (HH).

The soundings from Huanghua station are shown in the early morning (00:00 UTC, Figure 3a) and in the afternoon (1700 LST, Figure 3b). In the morning (00:00 UTC), the low convective available potential energy (CAPE) with 410 J·kg^{-1} and the large convective inhibition (CIN) with 130 J·kg^{-1} caused air parcels to struggle to reach the lifting condensation level (LCL) to form convection. As the environment evolves over time, the thermal–dynamical conditions became more unstable than in the morning; the CAPE increased to 1907 J·kg^{-1} and the CIN decreased to 24 J·kg^{-1} in the afternoon (09:00 UTC, Figure 3b). Moreover, the temperature lapse rate at the lower level (below 800 hPa) approached the dry adiabatic lapse rates, which means that te downdraft that originated from the level below 700 hPa remained negatively buoyant and accelerated until reaching 800 hPa. Thus, the temporal evolution of the prestorm environment was favorable for convective development.

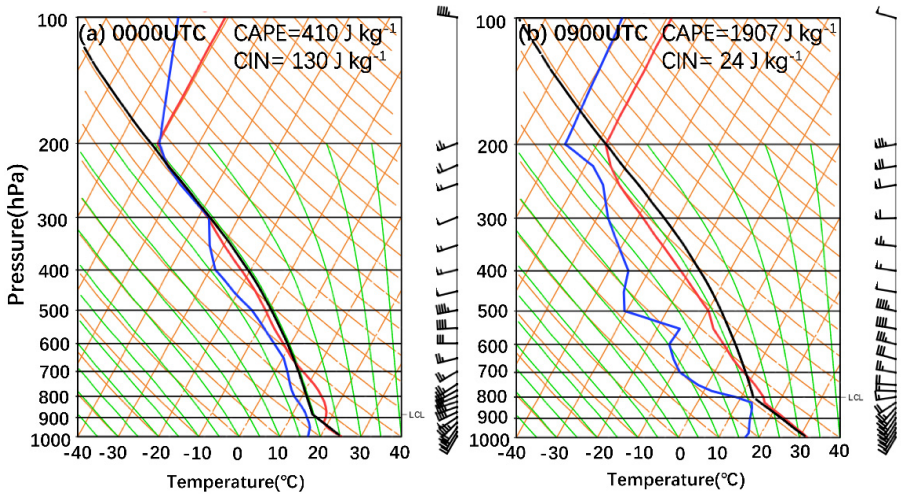

Figure 3. Skew T-logp diagram over Huanghua station at 00:00 UTC (**a**) and 09:00 UTC (**b**) on 10 June 2016. T (red solid line, unit: °C), Td (blue solid line, unit: °C), parcel T (black solid line, unit: °C) and wind (barb, unit: m·s^{-1}). The location of the sounding is marked in Figure 2.

4. Comparison of Evolution Characteristics of Cold Pools and GFs

This thunderstorm gale event was affected by two consecutive GFs over the BSB. The rearward GF (designated as RGF; 8 grade gale that appeared after passing GF) formed in the northwest region of Tianjin at 09:00 UTC 10 June and disappeared at 13:12 UTC in the Bohai Sea (Figure 1b). The gust speed at Xiqing station reached 17.2 m·s^{-1} after passing through the RGF (Figure 4a). The frontward GF (designated as FGF; 10 grade gale that appeared before passing GF) formed in the southwest region of Hebei Province at 12:12 UTC, entered the Bohai Sea, and disappeared around 15:00 UTC. The gust speed at Huanghua station reached 24.9 m·s^{-1} prior to the occurrence of the FGF (Figure 4b).

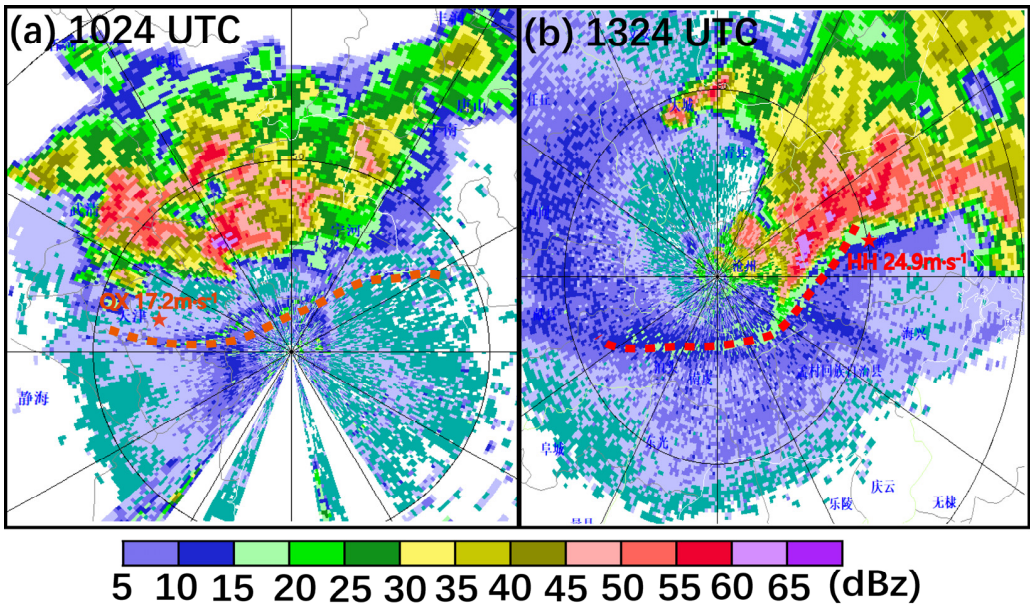

Figure 4. (**a**) Base reflectivity factors at an elevation of 1.5° in Tianjin (dBZ; shaded) on 10:24 UTC 10 June 2016. (**b**) Base reflectivity factors at an elevation of 1.5° in Canghzou (dBZ; shaded) on 13:24 UTC 10 June 2016. The color bar shows base reflectivity values in dBZ (the orange and red dashed lines refer to RPG and FGF, respectively.).

4.1. Comparison of Surface Thermal Fields

Observational studies of cold pools are still missing in some regions (e.g., North China), although the influence of cold pools is significant. The coastal North China region frequently encounters the mixing of moist oceanic airflows with dryer continental flows. Since cold pools are significantly influenced by near-surface moisture, it is necessary to study their characteristics based on AWS, where the surface temperature and dewpoint temperature differ between RGF and FGF. The air masses observed at 10:00 UTC could be classified into four distinct categories (Figure 5a): cool and dry air mass (quadrant I), and cold and very humid air mass (quadrant II) located at the rear of RGF, a more continental hot and very dry air mass (quadrant III), and a more maritime warm and moderately humid (quadrant IV) located at the front of RGF. This behavior suggests that the southwesterly inflow of boundary layer from quadrant III plays a crucial role in generating the RGF and causing destructive wind at 10:23 UTC within quadrant III, where surface parcels with a temperature dewpoint difference/temperature ratio of 16/33 °C are present.

Differing from RGF, only two air masses could be identified at 14:00 UTC (Figure 5b): the cold and very humid air masses were located at the rear of FGF, whereas warm and dry air masses were located at the front of FGF. The downdraft associated with the destructive winds of FGF appears to originate from the near-ground northeasterly inflow, originating from a cold and highly humid air mass with a temperature dewpoint difference/temperature ratio of 1/17 °C. These findings contradict previous studies that

suggest that the updrafts associated with destructive winds primarily draw their boundary layer inflow from warm and highly humid air masses [4].

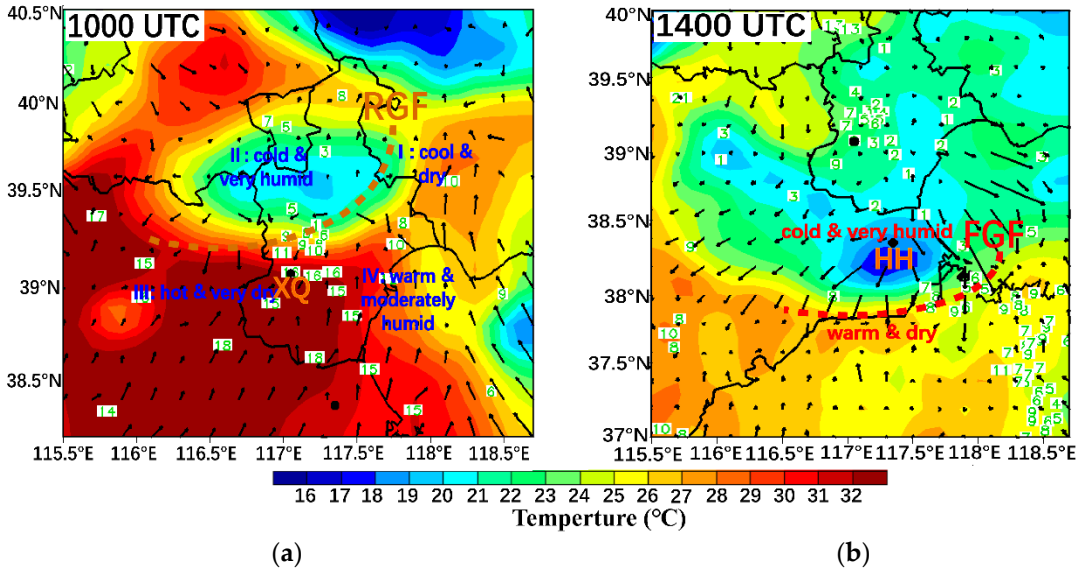

Figure 5. Mesoscale surface analysis at 10:00 UTC (**a**) and 14:00 UTC (**b**) 10 June 2016. The shaded region and green figure indicate surface temperature and dewpoint temperature difference, respectively, given in °C. Orange and red dashed lines refer to RGF and FGF, respectively.

Figure 6 shows the temporal evolutions of surface meteorological elements during the passage of the two GFs. The surface pressure typically begins to rise posterior to the passage of RGF and prior to the cold pool passage (Goff [17]). Therefore, the surface pressure prior to the arrival of the cold pool was determined by identifying the minimum surface pressure during the 32 min period prior to the wind shift (Figure 6a). RGF conforms to the structural characteristics of the traditional GF model [59]. However, unlike RGF, the surface pressure of FGF decreased rapidly after surging, exhibiting a "high-pressure nose", and the temperature dropped from 30.0 °C to 17.9 °C (Figure 6b). According to the theory, a stronger temperature difference between the boundary and ambient air leads to higher wind speeds behind the two air masses. These findings suggest that RFG exhibited a stronger relationship between temperature decrease and wind speed increase compared to FGF (with respective values of 6.9 °C and 17.2 m·s^{-1} for RGF, versus 12.1 °C and 24.9 m·s^{-1} for FGF).

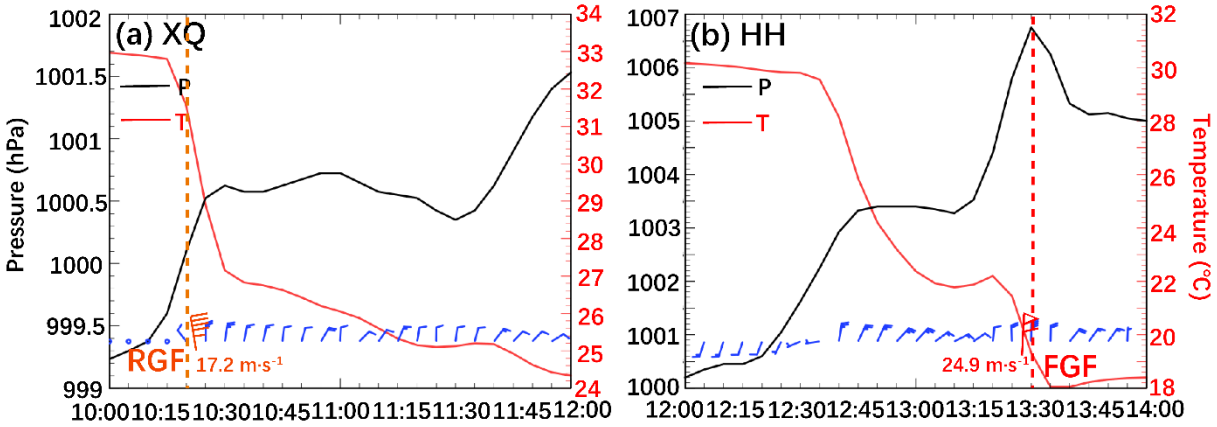

Figure 6. Variation in surface pressure (black line), temperature (red line), and wind from automatic weather observations on 10 June 2016. (**a**) Xiqing station; (**b**) Huanghua station. Orange and red numbers represent the gust wind speed; orange and red dashed lines refer to the time at which RGF and FGF passed by, respectively.

4.2. Comparison of Evolution Characteristics of Cold Pool GFs

To investigate the evolutionary characteristics of cold pool GFs, we utilized the mean perturbation temperature field, which is obtained by subtracting the horizontal mean prior to calculating the average as a representation of the cold pool structure [55]. From the surface meteorological elements, it can be seen that the near-surface cold pool (RGF-CP; shown in Figure 7a), accompanied by RGF, induces an anallobaric region of 3 hPa within one hour and a temperature perturbation center of −12 °C at 10:00 UTC 10 June. A divergent wind field forms at the rear of the cold pool, while a warm and moist inflow leads to a katallobaric region at its front. At 11:00 UTC, the characteristics of a mesoscale pressure field start to appear in RGF, including the katallobaric region ahead of the front, the anallobaric region on the rear of the front, and the katallobaric region in the rear-flow (Figure 7b). A strong echo develops toward the 1 h katallobaric center, resulting in a temperature gradient across the RGF with a value of 1.9 °C·(10 km)$^{-1}$, and the pressure gradient reaches 7.4 hPa·(10 km)$^{-1}$. The speed zone of the strong wind on the surface appears in the area with high isobars and isotherm gradients.

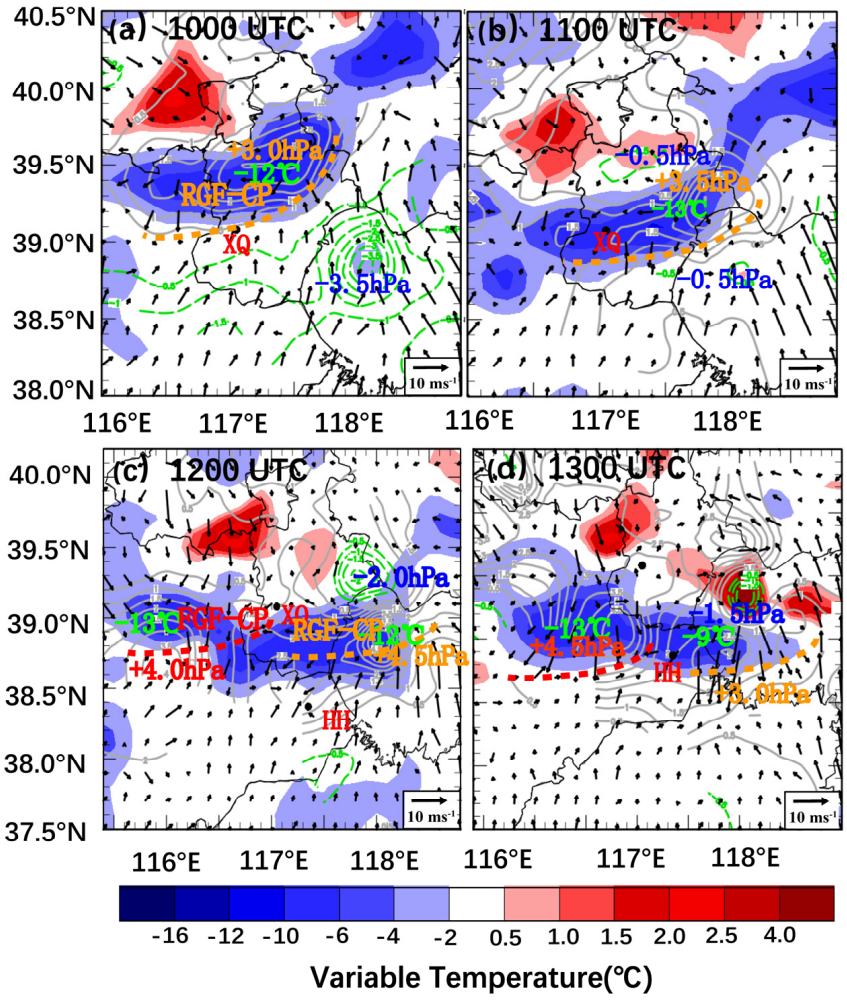

Figure 7. Surface observations on 10 June 2016. The solid line represents a 1h allobar with an interval of 0.5 hPa. The shaded region indicates 1 h variable temperature. Orange and red dashed lines refer to RGF and FGF, respectively. (**a**) 1000 UTC; (**b**) 1100 UTC; (**c**) 1200 UTC; (**d**) 1300 UTC.

At 1200 UTC, as the near-surface cold pool (FGF-CP in Figure 7c) gradually expands and approaches the RGF-CP, the two GFs prior to the cold pools collide. Unlike the RGF, the warm and dry-air masses occurred prior to FGF (Figure 5b), so no katallobaric region appeared ahead of FGF. At 13:00 UTC, the FGF-CP was further expanded and strengthened,

resulting in an anallobaric center of 4.5 hPa. The collision and merging of the two cold pools further enhanced the temperature gradient near the surface. In addition to the intense lifting induced by the collision of cold pools (Meyer and Haerter [43]), the merging of the two cold pools also influenced the horizontal temperature field, which, in turn, caused air condensation and subsidence. The negative temperature-change center corresponds to the speed zone of the strong wind on the surface (Figure 7c,d).

The shallower and weaker cold pool of RGF leads to a correspondingly weaker outflow and downdraft, while the stronger wind and vertical shear of FGF generate more robust and organized downdrafts, resulting in a deeper cold pool with a large associated outflow. This enhanced outflow subsequently induces larger downdrafts ahead of the cold pool, thereby elucidating the formation of a more intense surface gale.

5. Implications of Cold Pools on the GFs

Since observations are limited to discrete surface AWS data, we now examine the potential role of cold pools on the evolution of GFs by utilizing high-resolution VDRAS data.

5.1. Intensity of GFs

As GFs often behave like density or gravity currents (Bryan and Rotunno [60]), on their leading edge, a nose-like shape forms, which tends to be deeper and marks the region with the strongest lift and convergence between the outflow and environmental air. The vorticity maxima along the GFs are responsible for the MVs (Atkins and Laurent [61]); therefore, an intensity is seen in the MVs along the GFs. Figure 8 presents the detailed evolution of MVs at 200 m AGL in association with GFs using the VDRAS data. The southwest flow at 200 m AGL within the RGF reaches speeds of 10–12 $m \cdot s^{-1}$, facilitating the continuous transport of warm and humid air from the near surface to the region where thunderstorms develop. Within the RGF front, there exists a robust upward motion characterized by intense warmth and humidity, with a maximum vertical velocity reaching 1.8 $m \cdot s^{-1}$ (Figure 9a). Note that several MVs develop along the leading edge of the RGF (Figure 8a), with a diameter of 5~15 km, maximum vorticity of 2.4 $\times$ 10^{-5} s^{-1}, and vertical depth of 800 m. However, as depicted in the vertical cross-sections for the vortex illustrated in Figure 9, these vortices persist at shallow depths (less than 1 km) and do not exhibit any association with midlevel updraft (Table 1).

Table 1. Comparing structure and cold pool characteristics for RGF and FGF.

Element Features	**RGF**			**FGF**		
Representative station gust wind ($m \cdot s^{-1}$)		Xiqing 17.2			Huanghua 24.9	
Evolution time (UTC)	1012	1036	1054	1312	1324	1342
Intensity of GFs ($10^{-5} \cdot s^{-1}$)	2.4	2.4	2.0	3.6	4.0	4.4
Intensity of cold pools ($°C \cdot (10\ km)^{-1}$)	24	22	22	26	32	28
Depth of cold pools (m)	600	900	800	1400	1450	1600
Propagation speed of cold pools ($m \cdot s^{-1}$)	8.4	18.1	19.5	21.3	28.2	31.0

With the passage of time, the southwesterly flow at 200 m AGL in front of the FGF gradually shifted to a southeasterly flow. The continuous transport of cold and moist air from nearby formations contributed to the development of a robust cold pool and a distinct outflow boundary at its forefront. The intensification of this cold pool resulted in enhanced vertical wind shear, promoting sustained upper- and lower-level rotation and generating significant horizontal vorticity. Notably, the maximum convergence-induced updraft speed reached 2.4 $m \cdot s^{-1}$ (Figure 9b). Some significant MVs can also be found in association with the FGF, while the strongest vortice "1" with 3.6 $\times$ 10^{-5} s^{-1} is located at the forefront of the FGF (identified in Figure 8d–f).

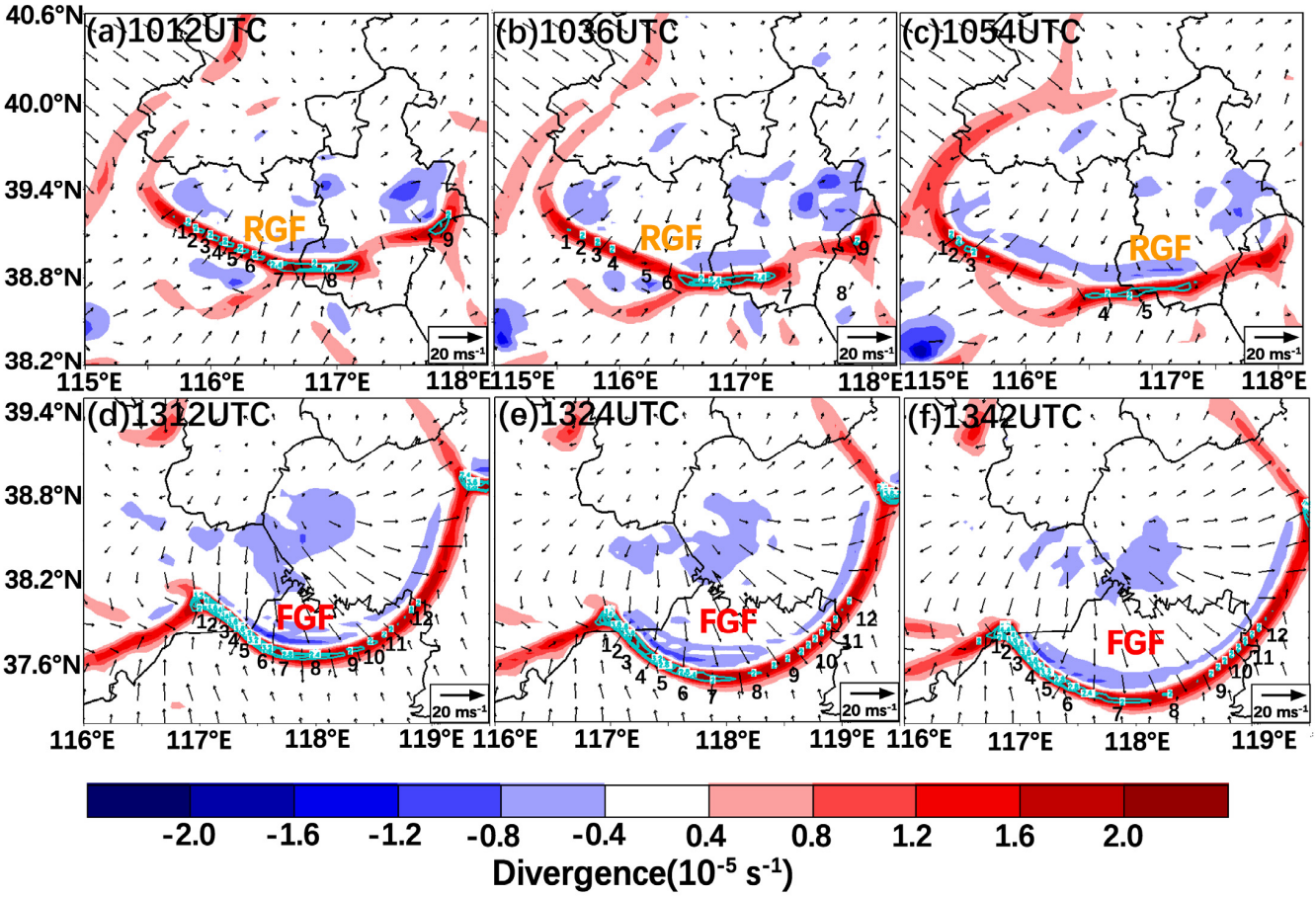

Figure 8. Horizontal wind (vector, unit: m·s^{-1}), vorticity (blue solid, unit: 10^{-5}·s^{-1}) and divergence (shaded, unit: 10^{-5}·s^{-1}, it is positive for convergence and negative for divergence) at a height of 200 m of VDRAS data on 10 June 2016. (**a**) 1012 UTC; (**b**) 1036 UTC; (**c**) 1054 UTC; (**d**) 1312 UTC; (**e**) 1324 UTC; (**f**) 1342 UTC.

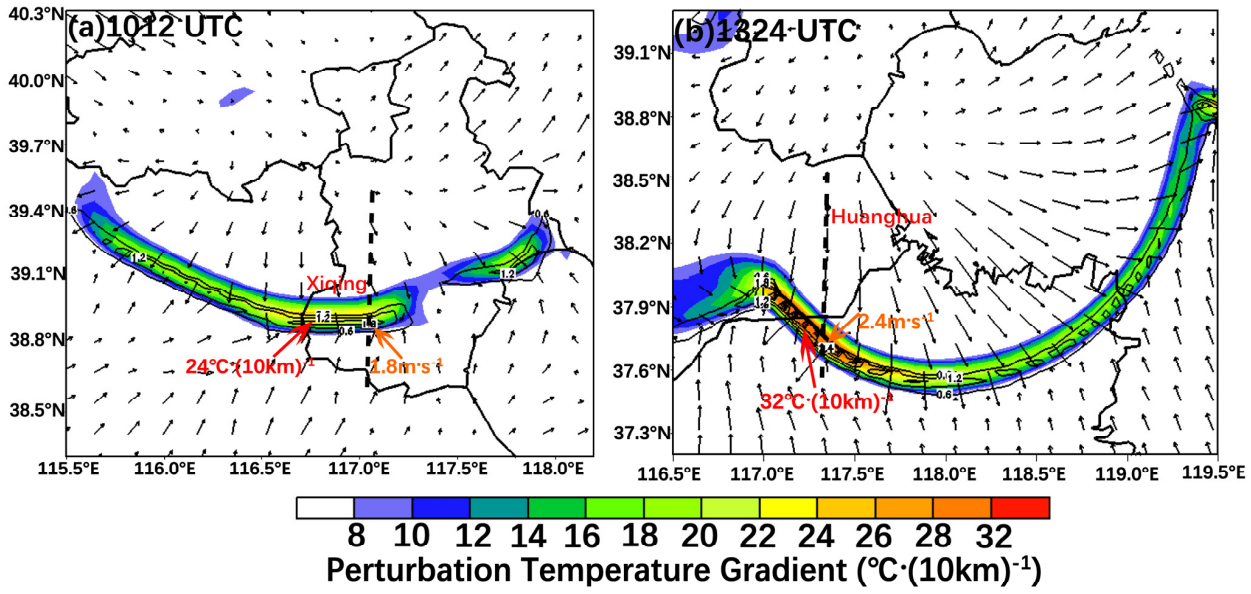

Figure 9. Horizontal wind (m·s^{-1}), perturbation temperature gradient (°C · (10 km)$^{-1}$; shaded) at a height of 200 m, and vertical velocity (m·s^{-1}; black contours) at 600 m of VDRAS data on 10 June 2016. (**a**) 1012 UTC; (**b**) 1324 UTC.

5.2. Intensity of Cold Pools

Figure 9 shows that there is an arc-shaped structure present in the zone with a large value for disturbance temperature gradient. The strongest temperature gradient caused by the RGF is 22–24 °C·(10 km)$^{-1}$, which is found in the protuberance of the front edge along its moving direction. The maximum ascending speed at the leading edge of RGF is 1.8 m·s^{-1}, located in the left front along its moving direction. The enhancement of the cold pool leads to a strong wind shear on the leading edge, which is conducive to maintaining the upper and lower rotation and forming a strong horizontal vorticity. The convergence zone corresponding to RGF can be clearly seen in the near surface, and the maximum convergence rising speed is 1.8 m·s^{-1} (Figure 9a). The destructive wind appears 5 min after the passage of RGF, which is caused by the discontinuous interfaces in the horizontal and vertical directions, where the density flow consists of pressure and temperature gradients exist, resulting from the descending strong cold air and warm humid air near the surface.

Figure 10 shows a vertical profile of the horizontal wind speed, divergence, and V-W composite fields along the dashed line (i.e., the location of the GFs in Figure 9). RGF exhibits opposite characteristics, with a divergence below 0.6 km and convergence over 0.6 km. The descending motion and ascending motion on the rear of RGF constitute a vertical circulation. The extending height of the ascending branch reached about 1.8 km, which coincides with the maximum height of development (1.7 km) observed by the Doppler weather radar (figure omitted). The maximum ascending speed at the leading edge of RGF is 1.8 m·s^{-1} (Figure 9a). The maximum horizontal wind speed at the height of 0.2 km around the rear of the RGF reaches 18 m·s^{-1}, which is basically equal to the maximum gust speed it caused on the surface caused. The convergence in RGF is noticeably weaker than that in FGF, which is consistent with the comparatively weaker southwesterly environmental flow, as well as the presence of cold pools and a weaker outflow. The diminished outflow and the associated weakened convergence elucidate why the thunderstorm parent in RGF dissipated upon crossing BSB, whereas the thunderstorm parent in FGF intensified during its passage over BSB. The strong southwest inflow at the front of PGF and the strong northeast inflow at the back constitute the forward counter circulation and the positive circulation at the back of PGF, respectively (Figure 10b). The forward inflow and the backward inflow are strengthened at the same time, resulting in the continuous strengthening of the vertical circulation of PGF and the corresponding, simultaneous vertical wind shear. This dynamic process is conducive to the organizational development of the convective storm and the strengthening of the downdraft in the storm, while the stronger wind and vertical shear of FGF generate more robust and organized downdrafts, resulting in a deeper cold pool with a large associated outflow. This enhanced outflow subsequently induces larger downdrafts ahead of the cold pool, thereby elucidating the formation of a more intense surface gale.

The disturbance temperature gradient reached a maximum value of 30–32 °C·(10 km)$^{-1}$, located at the front right along the moving direction of FGF (Figure 9b). The large-value zone of the disturbance temperature gradient corresponds well with its vertical speed and wind speed. The FGF shows the convergent features in all layers (Figure 10b). The descending and ascending motion on the rear front constitute a vertical circulation, and the ascending branch extends to a height of around 2.6 km. The maximum ascending speed at the leading edge of FGF is 2.4 m·s^{-1} (Figure 9b), whereas it is stronger in the RGF. This difference corresponds to the intensities of the GFs, which are significantly different. The maximum horizontal wind speed at the height of 0.2 km is 27 m·s^{-1}, which is slightly stronger than the maximum gust speed observed on the ground (24.9 m·s^{-1}). Provod et al. [37] showed that the intensity of the cold pool is consistent with that of the ground gale. The difference between the intensities of the two thunderstorm gales also confirm that the intensity of the cold pool after FGF (11.4 °C), which is larger than that after RGF (6.9 °C), eventually produces a stronger thunderstorm gale.

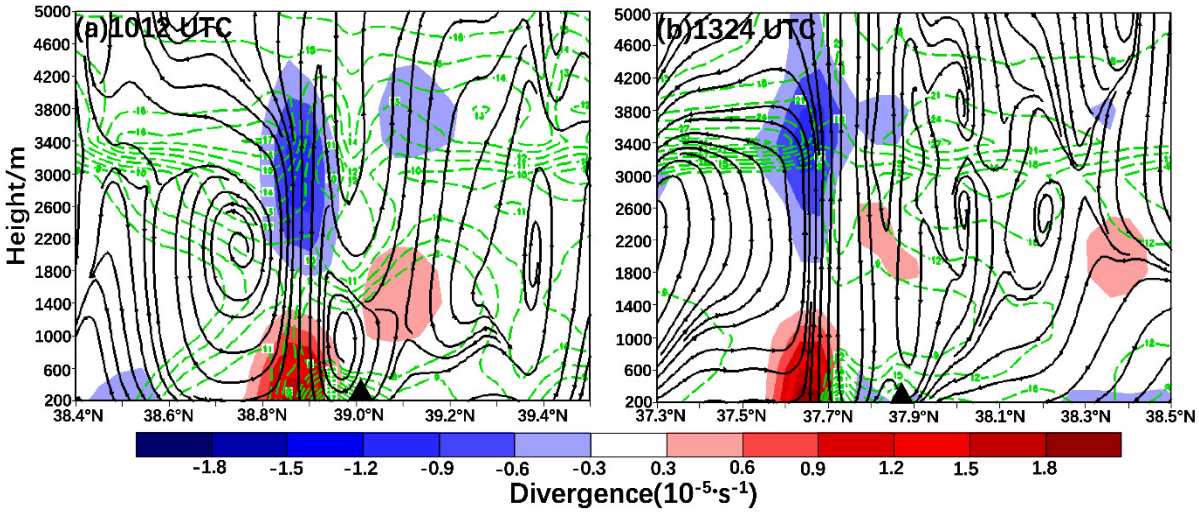

Figure 10. Cross-sections of horizontal wind speed (green dashed line, unit: m·s^{-1}); divergence (shaded, unit: 10^{-5}·s^{-1}; positive for convergence and negative for divergence); V-w (w amplified 50 times) for VDRAS data on 10 June 2016. (**a**) Along 117.05° E at 10:12 UTC. ▲: position of RGF. (**b**) Along 117.35° E at 13:42 UTC. ▲: position of FGF.

5.3. Depth of Cold Pools

The depth, size, and intensity of cold pools are contingent upon the environmental properties and downdrafts that nourish them. Conversely, the characteristics of downdrafts rely on both the environment and the attributes of associated updrafts. The idealized numerical modeling conducted by Marion and Trapp [62] suggests a strong correlation between the depth of the cold pool and the widths of the updrafts and downdrafts in supercell thunderstorms and their environments. These dimensions are ultimately governed by various storm-related factors, including CAPE, vertical wind shear, and mixed-layer depth. To identify these differences in the cold pool depth and vertical motion for the two types of GFs, the temperature perturbations of <-18 °C at the lower level are shown in Figure 11. The FGF parent thunderstorm generates a significantly deeper cold pool compared to the RGF (0.6 km for RGF and 1.6 km for FGF). The divergence in cold pool characteristics between the two types of GFs is also evident from the variability observed in surface temperature (Figure 6). The convection-induced downdraft in FGF is attributed to the strong dry and cold northwesterly inflow, resulting in a cold pool that resembles the typical vertical structure of GF [15,59]. In comparison, RGF exhibits a much weaker updraft and downdraft (Figure 11), leading to a shallower and weaker cold pool.

5.4. Propagation Speed of Cold Pools

The above analyses suggest that the dynamics of cold pools may play a crucial role in the evolution of the FGF and RGF. Richter et al. [4] emphasized that when the outflow from a cold pool interacts with the ground, it accelerates outward into less dense ambient air, exhibiting characteristics similar to those of a spreading gravity current. Hutson et al. [63] employed a numerical model to quantify the correlation between outflow thermodynamic deficit and gust front structure, revealing that, in a sheared flow, the edge of a strong cold pool was less inclined than that of a weaker cold pool. Furthermore, a cold pool in weak ambient shear exhibited a steeper slope compared to the same cold pool in stronger shear.

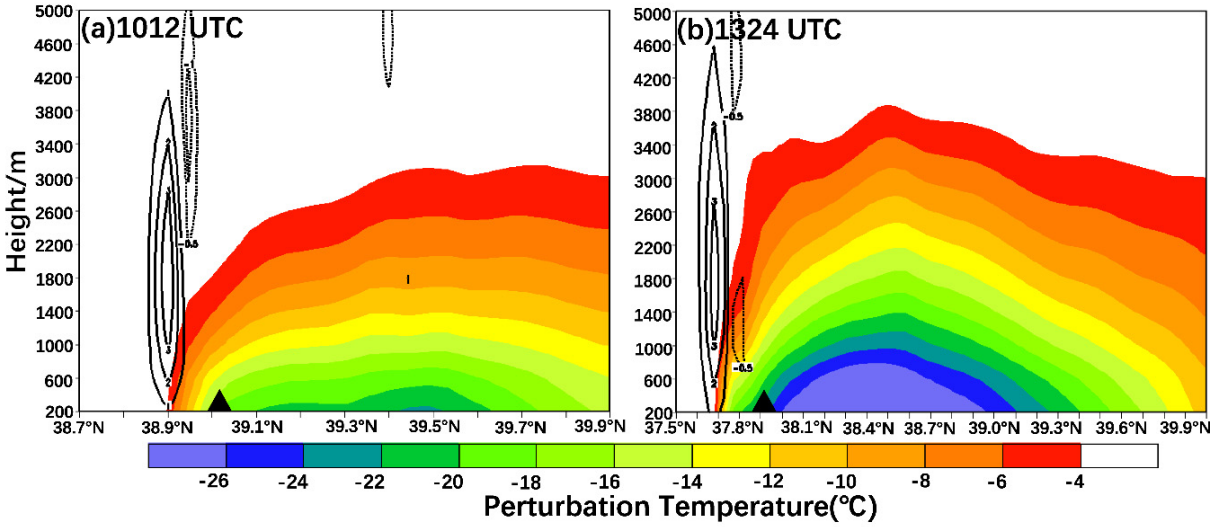

Figure 11. Cross-section of perturbation temperature (shaded, unit: °C); vertical velocity (black line, unit: m·s^{-1}, positive for ascending and negative for descending) of VDRAS data on 10 June 2016. (**a**) Along 117.05° E at 10:12 UTC. ▲: position of RGF. (**b**) Along 117.35° E at 13:42 UTC. ▲: position of FGF.

The propagation speed of GFs is primarily determined by the cold pool depth, H, and density difference, Δρ, compared to ambient air. This behavior aligns with both theoretical predictions for gravity currents and Benjamin's derived propagation speed for cold pool boundaries [64]:

$$C \sim \sqrt{2gH\frac{\Delta\rho}{\rho}} \sim \sqrt{2\frac{\Delta P}{\rho}} \quad (1)$$

where ρ is the density of the cold pool air; ΔP is the pressure difference. The propagation speed of RGF and FGF determined using Equation (1) are shown in Figure 12. The propagation speed of RGF is the value of 19.46 m·s^{-1} at 1030 UTC, about 7 min after the onset of the surface destructive wind, whereas the peak speed of FGF at 1330 UTC was 31.04 m·s^{-1} (Figure 12b). Both the propagation speeds of GFs exceeded that of the surface wind. This contradicts several studies that demonstrated that the maximum wind gust was larger than the GF propagation speed [17,19,59]. These findings suggest that the downdraft decelerates near the ground as it interacts with the cold pool, indicating that the theoretical propagation speed of the cold pool in Figure 12 overestimates realistic surface winds.

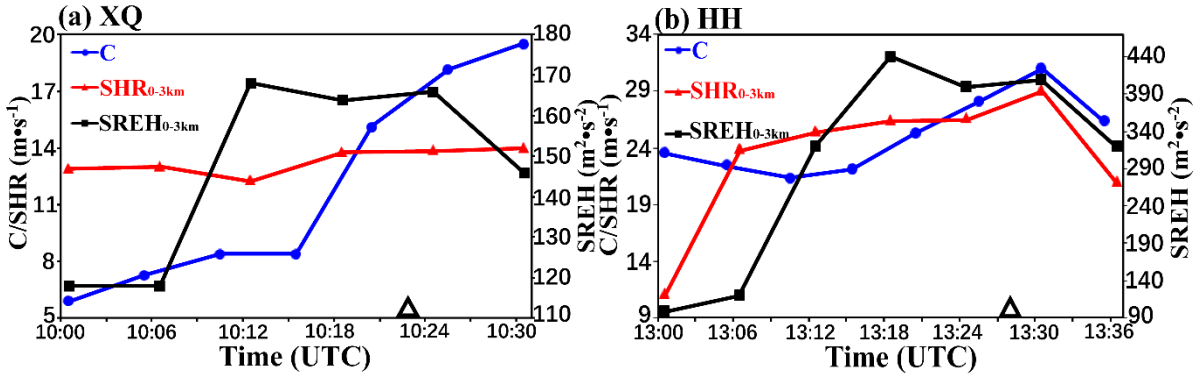

Figure 12. Time series of cold pool propagation speed (blue solid, unit: m·s^{-1}), 0–3 km AGL shear wind shear (red solid, unit: m·s^{-1}) and 0–3 km AGL storm-relative environmental helicity (black solid, unit: m^2·s^{-2}) during the passage of two GFs. Δ: The time of surface destructive winds. (**a**) Xiqing; (**b**) Huanghua.

The RKW88 [28] theory addresses the interaction between cold pool and shear, elucidating how shear influences the transformation of transient thunderstorms into a persistent line of cells. The RKW "optimal" state is shown when C/Δu approaches 1 (Δu represents the magnitude of low-level ambient vertical wind shear), ensuring an upright configuration for the system and generating maximum lifting at the leading edge of the cold pool (Weisman and Rotunno [65]). The time series of vertical wind shear between 0 and 3 km AGL across Xiqing and Huanghua station are shown as a curve in Figure 12. The C/Δu of RGF is 0.46 at 10:00 UTC, which means the thunderstorm tilted forward. After the cold pool developed quickly, its propagation speed was equal to the low-level shear at 1020 UTC, which is a closer match to the time of the surface gust (10:23 UTC). The cold pool reached a state where $C/\Delta u > 1$, indicating that the circulation associated with the cold pool surpassed that of the low-level shear, resulting in the displacement of the thunderstorm and its cooling zone rearward. This finding aligns with modeling results from RKW88 [28], which suggest that when the low-level shear across the depth of the cold pool is significantly lower than the speed of RGF propagation, similar dynamics occur. The fact that RGF was propagating away from the parent convection (figure omitted) indicates that the shear and speed of cold pool deviate significantly from RKW88's optimal conditions for convectively coupled circulations. In the case of RGF, a reduced vertical wind shear may be necessary to enhance the deep ascent along the leading edge of the elevated cold pool, although shear likely still plays a role in this ascent mechanism.

For FGF, C/Δu was ~2.1 at 13:00 UTC, falling within the range of values indicative of upright convection, which exceeded the theoretical optimal balance proposed by Weisman and Rotunno [65] by a factor of two. This ratio decreased to 1.1 at 13:30 UTC (Figure 12b), approaching the proposed optimal balance, indicating favorable conditions for an upright convective process. The vertical wind shear in the 0–3 km layer was measured at 29.2 $m \cdot s^{-1}$ during the occurrence of the FGF gust, which was significantly higher than that observed for RGF.

5.5. Implications of Cold Pools on the GFs

The helicity concept is based on the utilization of streamwise and crosswise vorticity to characterize the rotational character of a quasi-steady propagating updraft (Davies-Jones [64]). A study of the linearized vertical vorticity equation in an ambient, vertically sheared environment reveals that when an updraft propagates parallel to the mean shear vector, it will exhibit a mid-level vortex couplet, resulting in negligible net rotation. However, if the updraft propagates perpendicular to the mean vertical wind shear vector, it will display a preferred direction of rotation. Davies-Jones [66] derived this correlation analytically, based on a linear analysis of the equations of motion. The measure of this predicted correlation is commonly referred to as storm-relative environmental helicity (SREH), which quantifies twice the area enclosed by the hodograph and the storm-relative wind vectors, extending from the surface to a specified height [usually 3 km AGL; Davies-Jones [66]].

SREH provides the potential for the rotational characteristics of convective storms (Davies-Jones [66]), and is defined as follows:

$$SREH = \int_0^h k \times \frac{\partial V}{\partial z} \cdot (V - C) dz \quad (2)$$

where V is the environment wind vector, C is the storm motion vector, h is an assumed inflow depth, and k is a unit vertical vector.

Furthermore, the right-hand side of Equation (2) can be written as follows (Marion and Trapp [62]):

$$SREH = \sum_{n=0}^{N-1} [(u_{n+1} - C_x)(v_n - C_y) - (u_n - C_x)(v_{n+1} - C_y)] \quad (3)$$

where (u_n, v_n) is the environment wind at each level; (C_x, C_y) is the storm motion vector. We used h $\approx$ 3 km for the storm inflow coming from low levels. We estimated SERH according to the VDRAS data of Xiqing and Huanghua station. This was achieved using an estimated storm motion. It was decided to estimate mean storm motion at 75% of the mean profile radar speed and 30° to the right of the mean profile radar wind direction (Maddox [67]).

Time–height cross-sections of SREH are shown in Figure 12 and clearly illustrate two GF passages. After 10:06 UTC, the SREH in RGF gradually increased, and exceeded 164 $m^2 \cdot s^{-2}$ at 1018 UTC (Figure 12a). However, from 13:00 UTC to 13:18 UTC, SREH in FGF rapidly increased from 100 $m^2 \cdot s^{-2}$ to 440 $m^2 \cdot s^{-2}$ (Figure 12b). The differences in SHER between RGF and FGF are strongly correlated with the intensity of low-level vertical shear, as well as the enhanced propagation speed of the cold pool, which are associated with the structural characteristics of GFs at the boundary and the lower troposphere. Consequently, a larger low-level vertical shear and faster cold pool density flow result in increased SREH.

6. Summary and Discussion

On 10 June 2016, a destructive wind that occurred at the north coast of China was associated with a rearward gust front (RGF; 8 grade gale appeared after passing GF) and a frontward gust front (FGF; 10 grade gale appeared before passing GF) along CCs, which induced agriculture and port transportation economic losses in BSB, North China. By using multiple observation data and VDRAS data, we found that the intensity of GFs increased with cold pool strength, depth, and propagation speed.

Of particular significance is the configuration of cold pool and low-level vertical shear, which has a large impact on the structure and strength of GFs. The FGF gale, in which the propagation speed of the cold pool was equal to the low-level vertical shear, has a deeper structure and stronger destructive wind. On the other hand, the RGF gale, in which the cold pool was smaller than the FGF-cold pool, has a relatively shallower structure and weaker destructive wind. The MVs are generated just along the leading edge of GFs. However, some differences are evident as the strength and depth of the vertical wind shear increase, including a stronger, deeper, and more upright thunderstorm and a closer inherent correlation between the MVs and GFs. Due to the enhancement of MVs, strong low-level convergence and the updraft along FGF coordinate with the enhancement of the cold pool, aggravated low-layer instability, and rotation, which induce a stronger horizontal vorticity, finally leading to the rapid strengthening of the convective storm and surface gust.

There is an internal correlation between MVs and cold pools; the collision of MVs strengthened low-level convergence and updraft between these two GFs. Simultaneously, the consolidation of the two cold pools exacerbates low-layer instability and rotation, generating an intense horizontal vorticity that leads to rapid convective storm intensification. Dynamically, the interplay between horizontal vorticity generated by the GFs at the head of cold pools and vorticity from vertical wind shear results in a lift of the convection storm. The strong cooling near the ground leads to the strengthening of the cold pool, which in turn causes air condensation and subsidence. The local pressure sharply increases, and the negative buoyancy generated by the sinking air stream temperature is significantly lower than the ambient atmospheric temperature, which is enhanced, strengthening the sinking movement.

Additionally, the conceptual model should be explored to deepen our understanding of these two types of GFs. A conceptual model of a shallow(deep) cold pool is shown in Figure 13a,b. The stronger GFs and vertical shear generate stronger and more organized downdrafts compared with the weaker GFs, which in turn produce a deeper cold pool and a stronger associated outflow. The stronger outflow results in a more robust gust ahead of the cold pool, which explains the surface gust that appeared before the passing GF. In contrast, the cold pool produced in RGF is shallower and weaker, which results in a weaker outflow and surface gust. These results indicate that the downdraft forcing for FGF is

stronger than that for RGF, and FGFs have a more deepener structure and larger SREH than RGFs, resulting in a stronger thunderstorm gale.

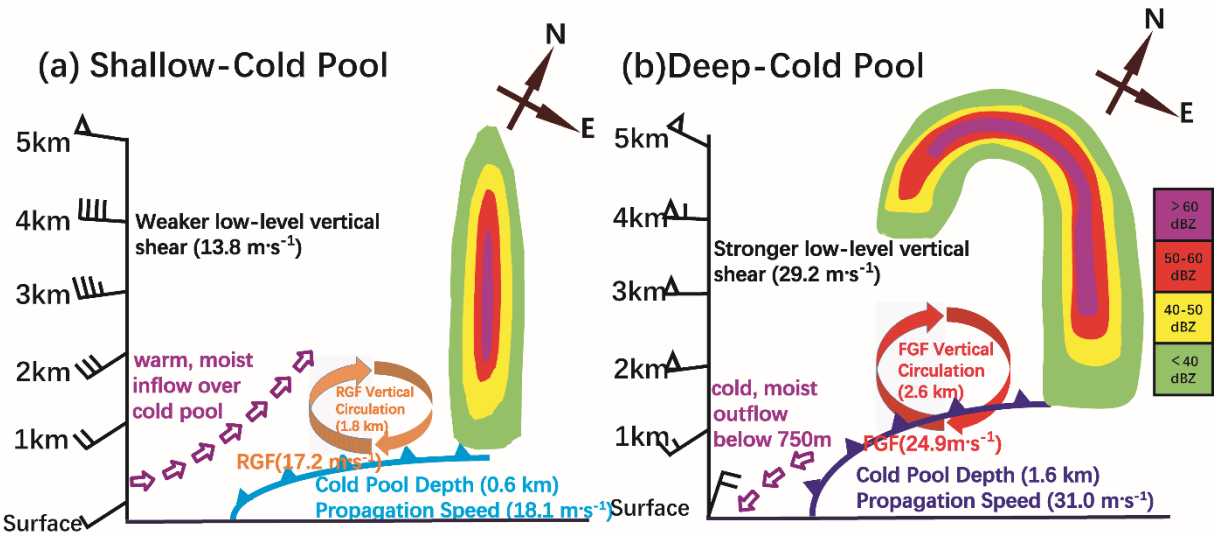

Figure 13. Schematic diagrams of the GFs, cold pools, and environmental wind for (**a**) RGF and (**b**) FGF gales. The shading corresponds to the composite radar reflectivity (dBZ).

Both RGF and FGF gales occur under the same large circulation (upper cold vortex), while the gale and GF sequences are obviously different, which brings uncertainty to the now-casting and early warning processes, leading to difficulties in the forecast. The disparities in the intensity of the two types of GFs, the sequential induction of surface gales, and the magnitude, depth, and propagation velocity of the associated cold pools signify variations in distinct gust fronts and their triggering capabilities. Similarities and differences can be found in the two GFs, which each have unique characteristics. On one hand, this reflects the diversity of GF gales. On the other hand, it leads to the question of "which one occurs first?" Whether the thunderstorm gale is caused by the GF or the GF is caused by the thunderstorm gale (including the downdraft) needs to be studied in greater detail.

Finally, the results from this study suggest that the strength, depth, and propagation speed of cold pools are influenced by a multitude of multiscale processes, which pose challenges for simultaneous observation using existing platforms. The accurate prediction of the movement becomes crucial for issuing disaster warnings once nascent convection is clearly initiated. The confluence point formed by the moving GFs is the source of dynamic forcing, and the intensity of the cold pools is closely associated with the GFs. However, the convective storm movement is affected by the atmospheric environment near the storm, so it is necessary to pay attention to the synthesis effect with the near-ground wind field. Therefore, it is imperative to conduct more idealized numerical simulations in order to investigate the development of cold pools in diverse environments. Additionally, since hydrometeor evaporation plays a significant role in driving cold pool formation, enhancing the representation of microphysics in models would also be advantageous. As our understanding the adverse and beneficial feedback induced by the outflow boundary (i.e., gust front) improves, undoubtedly our ability to forecast storm and GF intensity will also be enhanced.

Author Contributions: Conceptualization, C.X. and X.X.; methodology, X.X.; software, X.X.; validation, X.X.; formal analysis, C.X.; data curation, X.X.; writing-original draft preparation, C.X.; writing-review and editing, C.X. and X.X.; visualization, X.X.; supervision, C.X. and X.X. All authors have read and agreed to the published version of the manuscript.

Funding: The work was jointly supported by the Key Laboratory of Urban Meteorology, China Meteorological Administration, Beijing (LUM-2023-11), Open Research Fund for The Institute of Atmospheric Environment, China Meteorological Administration, Shenyangy (2023SYIAEKFMS05), China Meteorological Administration Review Special Summary (FPZJ2024-006) and Beijing Natural Science Foundation (8212026).

Institutional Review Board Statement: Not applicable.

Informed Consent Statement: Not applicable.

Data Availability Statement: The ERA5 data can be downloaded for free at websites https://cds.climate.copernicus.eu/cdsapp#!/dataset/reanalysis-era5-pressure-levels?tab=form (accessed on 11 February 2024) (Hersbach et al., 2020 [46]).

Conflicts of Interest: The authors declare no conflict of interest.

Abbreviations

GFs	Gust fronts
RGF	Rearward gust front
FGF	Frontward gust front
QLCS	Quasi-linear convective system
BE	Bow echo
CCs	Convective cells
MVs	Meso-γ-scale vortices
VDRAS	Variational Doppler Radar Data Assimilation System
4DVAR	Four-dimensional variational data assimilation
RKW88	Rotunno–Klemp–Weisman [26]
KHI	Kelvin–Helmholtz instability
IG	Internal gravity
LECP	Leading edge of the cold pool
BSB	Bohai Sea Bay
CI	Convection initiation
MCS	Mesoscale convection system
WRF	Weather Research and Forecast
AWS	Automatic weather station
AGL	Above ground level
CINRADs	China New-Generation Radars
CAPE	Convective available potential energy
CIN	Convective inhibition
LCL	Lifting condensation level
SREH	Storm-relative environmental helicity

References

1. Wilson, J.W.; Roberts, R.D. Lake Victoria thunderstorms: Radar-observed initiation and storm evolution modes. *Mon. Weather Rev.* **2022**, *150*, 2485–2502. [CrossRef]
2. Ma, R.Y.; Sun, J.H.; Yang, X.L. A 7-yr climatology of the initiation, decay, and morphology of severe convective storms during the warm season over North China. *Mon. Weather Rev.* **2021**, *149*, 2599–2612. [CrossRef]
3. Hurlbut, M.; Cohen, A. Environments of northeast U.S. severe thunderstorm events from 1999 to 2009. *Weather Forecast.* **2014**, *29*, 3–22. [CrossRef]
4. Richter, H.; Peter, J.; Collis, S. Analysis of a destructive wind storm on 16 November 2008 in Brisbane, Australia. *Mon. Weather Rev.* **2014**, *142*, 3038–3060. [CrossRef]
5. Fritsch, J.M.; Vislocky, R.L. Enhanced depiction of surface weather features. *Bull. Am. Meteorol. Soc.* **1996**, *77*, 491–506. [CrossRef]
6. Bai, L.Q.; Meng, Z.Y.; Huang, Y.; Zhang, Y.; Niu, S.; Su, T. Convection initiation resulting from the interaction between a quasi-stationary dryline and intersecting gust fronts: A case study. *J. Geophys. Res. Atmos.* **2019**, *124*, 2379–2396. [CrossRef]
7. Cui, X.Y.; Chen, M.X.; Qin, R.; Li, C.; Han, L. The roles of surface convergence line and upper-level forcing on convection initiation ahead of a gust front: A case study. *J. Geophys. Res. Atmos.* **2023**, *128*, e2022JD036921. [CrossRef]
8. Knupp, K.R. Observational analysis of a gust front to bore to solitary wave transition within an evolving nocturnal boundary layer. *J. Atmos. Sci.* **2006**, *63*, 2016–2035. [CrossRef]

9. Luo, X.; Xue, M.; Fei, J.F. Simulation and analysis of the initiation of a squall line within a Meiyu front system in East China. *Atmosphere* **2018**, *9*, 183. [CrossRef]
10. Waniha, P.F.; Roberts, R.D.; Wilson, J.W.; Kijazi, A.; Katole, B. Dual-polarization radar observations of deep convection over Lake Victoria Basin in East Afica. *Atmosphere* **2019**, *10*, 706. [CrossRef]
11. Marsham, J.H.; Parker, D.J. Secondary initiation of multiple bands of cumulonimbus over southern Britain. II: Dynamics of secondary initiation. *Q. J. R. Meteorol. Soc.* **2006**, *132*, 1053–1072. [CrossRef]
12. Zheng, J.; Abulikemu, A.; Wang, Y.; Kong, M.; Liu, Y. Convection initiation associated with the merger of an immature sea-breeze front and a gust front in Bohai Bay Region, North China: A case study. *Atmosphere* **2022**, *13*, 750. [CrossRef]
13. Zhang, N.; Wang, Y.; Lin, X. Mesoscale observational analysis of isolated convection associated with the interaction of the sea breeze front and the gust front in the context of the urban heat humid island effect. *Atmosphere* **2022**, *13*, 603. [CrossRef]
14. Friedrich, K.; Kingsmill, D.E.; Young, C.R. Misocyclone characteristics along Florida gust fronts during CaPE. *Mon. Weather Rev.* **2005**, *133*, 3345–3367. [CrossRef]
15. Wakimoto, R.M.; Murphey, H.V.; Davis, C.A.; Atkins, N.T. High winds generated by bow echoes. Part II: The relationship between the mesovortices and damaging straight-line winds. *Mon. Weather Rev.* **2006**, *134*, 2813–2829. [CrossRef]
16. Xu, X.; Xue, M.; Wang, Y. Mesovortices within the 8 May 2009 bow echo over the central United States: Analyses of the characteristics and evolution based on Doppler radar observations and a high-resolution model simulation. *Mon. Weather Rev.* **2015**, *143*, 2266–2290. [CrossRef]
17. Goff, R.C. Vertical structure of thunderstorm outflows. *Mon. Weather Rev.* **1976**, *104*, 1429–1440. Available online: https://journals.ametsoc.org/doi/pdf/10.1175/1520-0493(1976)104%3C1429:VSOTO%3E2.0.CO;2 (accessed on 11 February 2024). [CrossRef]
18. Luchetti, N.T.; Friedrich, K.; Rodell, C.E.; Lundquist, J.K. Characterizing thunderstorm gust fronts near complex terrain. *Mon. Weather Rev.* **2020**, *148*, 3267–3286. [CrossRef]
19. Luchetti, N.T.; Friedrich, K.; Rodell, C.E. Evaluating thunderstorm gust fronts in New Mexico and Arizona. *Mon. Weather Rev.* **2020**, *148*, 4943–4956. [CrossRef]
20. Wakimoto, R.M. The life cycle of thunderstorm gust fronts as viewed with Doppler radar and rawinsonde data. *Mon. Weather Rev.* **1982**, *110*, 1060–1082. [CrossRef]
21. Klingle, D.L.; Smith, D.R.; Wolfson, M.M. Gust front characteristics as detected by Doppler radar. *Mon. Weather Rev.* **1987**, *115*, 905–918. [CrossRef]
22. Harrison, S.J.; Mecikalski, J.R.; Knupp, K.R. Analysis of outflow boundary collisions in north-central Alabama. *Weather Forecast.* **2009**, *24*, 1680–1690. [CrossRef]
23. Karan, H.; Knupp, K. Radar and profiler analysis of colliding boundaries: A case study. *Mon. Weather Rev.* **2009**, *137*, 2203–2222. [CrossRef]
24. May, P.T. Thermodynamic and vertical velocity structure of two gust fronts observed with a wind Profile/RASS during MCTEX. *Mon. Weather Rev.* **1999**, *127*, 1796–1807. [CrossRef]
25. Cotton, W.R.; Bryan, G.; Van den Heever, S.C. *Storm and Cloud Dynamics*; Academic Press: Cambridge, MA, USA, 2011; Volume 99, 820p.
26. Martner, B.E. Vertical velocities in a thunderstorm gust front and outflow. *J. Appl. Meteorol.* **1997**, *36*, 615–622. [CrossRef]
27. Thorpe, A.J.; Miller, M.J.; Moncrieff, M.W. Two-dimensional convection in non-constant shear: A model of midlatitude squall lines. *Q. J. R. Meteorol. Soc.* **1982**, *108*, 739–762. [CrossRef]
28. Rotunno, R.; Klemp, J.B.; Weisman, M.L. A theory for strong, long-lived squall lines. *J. Atmos. Sci.* **1988**, *45*, 463–485. [CrossRef]
29. Weisman, M.L.; Klemp, J.B.; Rotunno, R. Structure and evolution of numerically simulated squall lines. *J. Atmos. Sci.* **1988**, *45*, 1900–2013. [CrossRef]
30. Weisman, M.L.; Rotunno, R. The use of vertical wind shear versus helicity in interpreting supercell dynamics. *J. Atmos. Sci.* **2000**, *57*, 1452–1472. [CrossRef]
31. Weckwerth, T.M.; Wakimoto, R.M. The initiation and organization of convective cells atop a cold-air outflow boundary. *Mon. Weather Rev.* **1992**, *120*, 2169–2187. [CrossRef]
32. Kingsmill, D.E. Convection initiation associated with a sea-breeze front, a gust front, and their collision. *Mon. Weather Rev.* **1995**, *123*, 2913–2933. [CrossRef]
33. Weisman, M.L.; Trapp, R.J. Low-level mesovortices within squall lines and bow echoes. Part I: Overview and dependence on environmental shear. *Mon. Weather Rev.* **2003**, *131*, 2779–2803. [CrossRef]
34. Trapp, R.J.; Weisman, M.L. Low-level mesovortices within squall lines and bow echoes. Part II: Their genesis and implications. *Mon. Weather Rev.* **2003**, *131*, 2804–2823. [CrossRef]
35. Atkins, N.T.; Laurent, M.S. Bow echo mesovortices. Part I: Processes that influence their damaging potential. *Mon. Weather Rev.* **2009**, *137*, 1497–1513. [CrossRef]
36. Kirsch, B.; Ament, F.; Hohenegger, C. Convective cold pools in long-term boundary layer mast observations. *Mon. Weather Rev.* **2021**, *149*, 811–820. [CrossRef]
37. Provod, M.; Marsham, J.H.; Parker, D.J.; Birch, C.E. A characterization of cold pools in the West African Sahel. *Mon. Weather Rev.* **2016**, *144*, 1923–1934. [CrossRef]
38. Hiris, Z.A.; Gallus, W.A., Jr. On the relationship of cold pool and bulk shear magnitudes on upscale convective growth in the Great Plains of the United States. *Atmosphere* **2021**, *12*, 1019. [CrossRef]

39. Parker, M.D. Self-organization and maintenance of simulated nocturnal convective systems from PECAN. *Mon. Weather Rev.* **2021**, *149*, 999–1022. [CrossRef]
40. Squitieri, B.J.; Gallus, W.A. On the changes in convection-allowing WRF forecasts of MCS evolution due to decreases in model horizontal and vertical grid spacing. Part I: Changes in cold pool evolution. *Weather Forecast.* **2022**, *37*, 1903–1923. [CrossRef]
41. Xue, M. Density currents in shear flows: Effects of rigid lid and cold-pool internal circulation, and application to squall line dynamics. *Q. J. R. Meteorol. Soc.* **2002**, *128*, 47–73. [CrossRef]
42. Borque, P.; Nesbitt, S.W.; Trapp, R.J.; Trapp, S.L.; Que, M. Observational study of the thermodynamics and morphological characteristics of a midlatitude continental cold pool event. *Mon. Weather Rev.* **2020**, *148*, 719–737. [CrossRef]
43. Meyer, B.; Haerter, J.O. Mechanical forcing of convection by cold pools: Collisions and energy scaling. *J. Adv. Model. Earth Syst.* **2020**, *12*, e2020MS002281. [CrossRef]
44. Hirt, M.; George, C.C.; Sophia, A.K.S.; Julien, S.; Rieke, H. Cold-pool-driven convective initiation: Using causal graph analysis to determine what convection-permitting models are missing. *Q. J. R. Meteorol. Soc.* **2020**, *146*, 2205–2227. [CrossRef]
45. Abulikemu, A.; Wang, Y.; Gao, R.; Wang, Y.; Xu, X. A numerical study of convection initiation associated with a gust front in Bohai Bay region, North China. *J. Geophys. Res. Atmos.* **2019**, *124*, 13843–13860. [CrossRef]
46. Hersbach, H.; Bell, B.; Berrisford, P.; Hirahara, S.; Horányi, A.; Muñoz-Sabater, J.; Nicolas, J.; Peubey, C.; Radu, R.; Schepers, D.; et al. The ERA5 global reanalysis. *Q. J. R. Meteorol. Soc.* **2020**, *146*, 1999–2049. [CrossRef]
47. Sun, J.; Crook, N.A. Dynamical and microphysical retrieval from Doppler radar observations using a cloud model and its adjoint. Part I: Model development and simulated data experiments. *J. Atmos. Sci.* **1997**, *54*, 1642–1661. [CrossRef]
48. Sun, J.; Crook, N.A. Dynamical and microphysical retrieval from Doppler radar observations using a cloud model and its adjoint. Part II: Retrieval experiments of an observed Florida convective storm. *J. Atmos. Sci.* **1998**, *55*, 835–852. [CrossRef]
49. Friedrich, K.; Kalina, E.A.; Aikins, J.; Gochis, D.; Rasmussen, R. Precipitation and cloud structures of intense rain during the 2013 Great Colorado Flood. *J. Hydrometeorol.* **2015**, *17*, 22–27. [CrossRef]
50. Tai, S.L.; Liou, Y.C.; Sun, J.; Chang, S.F. The development of a terrain-resolving scheme for the forward model and its adjoint in the four-dimensional Variational Doppler Radar Analysis System (VDRAS). *Mon. Weather Rev.* **2016**, *145*, 289–306. [CrossRef]
51. Crook, A.; Sun, J. Analysis and forecasting of the low-level wind during the Sydney 2000 Forecast Demonstration Project. *Weather Forecast.* **2004**, *19*, 151–167. [CrossRef]
52. Sun, J.; Chen, M.; Wang, Y. A frequent-updating analysis system based on radar, surface, and mesoscale model data for the Beijing 2008 forecast demonstration project. *Weather Forecast.* **2010**, *25*, 1715–1735. [CrossRef]
53. Sun, J. Convective-scale assimilation for radar data: Progress and challenges. *Q. J. R. Meteorol. Soc.* **2006**, *131*, 3439–3463. [CrossRef]
54. Chen, M.X.; Xiao, X.; Gao, F.; Lei, L.; Wang, Y.C.; Sun, J.Z. A case study and batch verification on high resolution numerical simulations of severe convective events using an analysis system based on rapid-refresh 4-D variational radar data assimilation. *Acta Meteorol. Sin.* **2016**, *74*, 421–441. (In Chinese) [CrossRef]
55. Xiao, X.; Sun, J.Z.; Chen, M.X.; Qie, X.S.; Ying, Z.M.; Wang, Y.C.; Ji, L. Comparison of environmental and mesoscale characteristics of two types of mountain-to-plain precipitation systems in the Beijing Region, China. *J. Geophys. Res. Atmos.* **2019**, *124*, 6856–6872. [CrossRef]
56. Wu, Y.; Sun, J.Z.; Ying, Z.; Xue, L.; Chen, D.; Lin, W. Effects of local-scale orography and urban heat island on the initiation of a record-breaking rainfall event. *J. Geophys. Res. Atmos.* **2021**, *126*, e2021JD034839. [CrossRef]
57. Zhang, L.N.; Sun, J.Z.; Ying, Z.M.; Xian, X. Initiation and development of a squall line crossing Hangzhou Bay. *J. Geophys. Res. Atmos.* **2021**, *126*, e2020JD032504. [CrossRef]
58. Xiao, X.; Sun, J.; Ji, L.; Zhang, L.; Ying, Z.; Chen, Z. A study on local-scale thermal and dynamical mechanisms in the initiation of a squall line under weak forcing. *J. Geophys. Res. Atmos.* **2022**, *127*, e2021JD035561. [CrossRef]
59. Mahoney, W.P. Gust front characteristics and the kinematics associated with interacting thunderstorm outflows. *Mon. Weather Forecast Rev.* **1988**, *116*, 1474–1491. [CrossRef]
60. Bryan, G.H.; Rotunno, R. Gravity currents in a deep anelastic atmosphere. *J. Atmos. Sci.* **2008**, *65*, 536–566. [CrossRef]
61. Atkins, N.T.; Laurent, M.S. Bow echo mesovortices. Part II: Their genesis. *Mon. Weather Rev.* **2009**, *137*, 1514–1532. [CrossRef]
62. Marion, G.R.; Trapp, R.J. The dynamical coupling of convective updrafts, downdrafts, and cold pools in simulated supercell thunderstorms. *J. Geophys. Res. Atmos.* **2019**, *124*, 664–683. [CrossRef]
63. Hutson, A.; Weiss, C.; Bryan, G. Using the translation speed and vertical structure of gust fronts to infer buoyancy deficits within thunderstorm outflow. *Mon. Weather Rev.* **2019**, *147*, 3575–3594. [CrossRef]
64. Weisman, M.L. The genesis of severe, long-lived bow echoes. *J. Atmos. Sci.* **1993**, *50*, 645–670. [CrossRef]
65. Weisman, M.L.; Rotunno, R. "A theory for strong long-lived squall lines" revisited. *J. Atmos. Sci.* **2004**, *61*, 361–382. [CrossRef]
66. Davies-Jones, R.P. Streamwise vorticity: The origin of updraft rotation in supercell storms. *J. Atmos. Sci.* **1984**, *41*, 2991–3006. [CrossRef]
67. Maddox, R.A. An evaluation of tornado proximity wind and stability data. *Mon. Weather Rev.* **1976**, *104*, 133–142. [CrossRef]

Disclaimer/Publisher's Note: The statements, opinions and data contained in all publications are solely those of the individual author(s) and contributor(s) and not of MDPI and/or the editor(s). MDPI and/or the editor(s) disclaim responsibility for any injury to people or property resulting from any ideas, methods, instructions or products referred to in the content.